An Asymptotic Closed-Form Representation for the Grounded Double-Layer Surface Green's Function

M. A. Marin, *Member, IEEE,* and Prabhakar H. Pathak, *Fellow, IEEE*

Abstract—**In this paper, an efficient closed-form asymptotic representation for the grounded double-layer (substrate-superstrate) Green's function is presented. The formulation is valid for both source (a horizontal electric dipole) and observation points anywhere inside the superstrate or at the interfaces. The asymptotic expressions are developed via a steepest descent evaluation of the original Sommerfeld-type integral representation of the Green's function, and the large parameter in this asymptotic development is proportional to the lateral separation between source and observation points. The asymptotic solution is shown to agree with the exact Green's function for lateral distances even as small as a few tenths of the free-space wavelength, thus constituting a very efficient tool for analyzing printed circuits/antennas. Also, since the asymptotic approximation gives separate contributions pertaining to the different wave phenomena, it thus provides physical insight into the field behavior, as shown through the examples.**

I. Introduction

THE grounded double-layer (substrate-superstrate) configuration is of increasing interest in printed circuit/antenna technology. It has been demonstrated in [1] and [2] that, by properly choosing the layer thicknesses and material parameters, significant improvements can be achieved in the performance of the printed antennas, including the reduction or elimination of surface waves, which is a subject of primary concern when dealing with large arrays of printed elements. Also, a double-layer structure allows for the separation of active circuitry and radiating patches in hybrid or monolithic integrated circuit technologies. These potential advantages lead to the need for accurate, "full-wave" analysis of such structures.

So far, the most commonly used approach to solve these problems (in single or double layers) has been the solution of the corresponding electric field or mixed potential integral equation (EFIE or MPIE), via the method of moments [3]–[8]. However, two different techniques have been applied to evaluate the elements of the moment method (MM) mutual impedance matrices. One of these is the spectral domain approach [4], [6], [7], which has the advantage of using simple formulas for the spectral representation of the Green's function, but requires numerical integration over the entire spectral plane. On the other hand, for the spatial domain method [3], [5], [8] the range of integration is restricted to the area of each subdomain or basis function, but the Green's function is expressed in terms of Sommerfeld-type integrals, which must be numerically evaluated at each spatial point. It is clear that both methods require a fairly large amount of computer time. Moreover, since both spectral and spatial integrands contain terms that oscillate faster for increasing separation between subdomains, the numerical integrations become very inefficient when computing the MM mutual coupling between widely separated basis functions. Also, if the spatial size of the basis functions is small, their transforms extend farther in the spectral domain, thus adding inefficiency to the numerical integration when the spectral domain approach is employed.

To overcome these limitations, we propose the use of an asymptotic closed-form representation of the Green's function, which makes the mutual coupling computation in the spatial domain extremely efficient. Such an asymptotic representation has already been obtained for the single-layer case [9]–[11], and was found to provide excellent results even for very small distances between source and observation points (usually down to a few tenths of the free-space wavelength). As an extension to the above work, the purpose of this paper is to develop an accurate asymptotic closed-form representation for the Green's function of a grounded double layer planar structure, as well as to show some of its advantages.

A further extension to include multilayers does not appear straightforward. The development of the closed form asymptotic result requires one to evaluate certain derivatives of the integrand present in the Green's function integral; such an evaluation becomes complicated for multilayers because in this case the integrand itself becomes rather complicated. It is for this reason that an asymptotic treatment of the more general, grounded multilayer Green's function has not been attempted here; only the special double layer case, which is of sufficient practical interest, is considered in this paper.

This paper is organized as follows. Section II presents the formulation of the substrate-superstrate Green's func-

Manuscript received October 28, 1988; revised September 26, 1991. This work was supported in part by Joint Services Electronics Program under Contract N00014-88-K-0004 and The Ohio State University Research Foundation.

M. A. Marin is currently with Ingenieria de Radiofrecuencias, 28035 Madrid, Spain; he was with the Ohio State University, Electroscience Laboratory, Columbus, OH 43212.

P. H. Pathak is with The Ohio State University, Electroscience Laboratory, Columbus, OH 43212.

IEEE Log Number 9204904.

tion in terms of Sommerfeld-type integrals for a horizontal Hertzian dipole embedded in the superstrate. Section III discusses the number and location of the relevant poles of the structure. The asymptotic evaluation of the original Sommerfeld integrals is carried out in Section IV. Finally, Section V presents numerical results showing the accuracy of the new asymptotic representation. It will be shown how the asymptotic formulas provide not only computational efficiency, but also physical insight into the field behavior. An $e^{+j\omega t}$ time dependence for the fields and sources is assumed and suppressed in the following analysis.

II. Formulation

Consider an infinitesimal $\hat{x}$-directed electric dipole at (x', y', z') embedded in the superstrate of a planar grounded double-layer configuration, as shown in Fig. 1. We are interested in calculating the $\hat{x}$- and $\hat{y}$-direction electric fields at any observation point (x, y, z) in the superstrate including the interfaces ($0 \le z, z' \le d_2$). These fields can be written as follows:

$$E_{xx} = \frac{-1}{2\pi\omega\epsilon_2}\left\{k_2^2 U + \frac{\partial^2}{\partial x^2}[U - W]\right\} \tag{1}$$

$$E_{yx} = \frac{-1}{2\pi\omega\epsilon_2}\left\{\frac{\partial^2}{\partial x\,\partial y}[U - W]\right\} \tag{2}$$

where

$$U = \int_0^\infty F^U(\xi) J_0(\rho\xi)\, d\xi \tag{3}$$

$$W = \int_0^\infty F^W(\xi) J_0(\rho\xi)\, d\xi \tag{4}$$

J_0 being the zeroth-order Bessel function

$$\rho = \sqrt{(x - x')^2 + (y - y')^2} \tag{5}$$

the lateral separation between source and field points. The wavenumbers in media 1 and 2 are defined as $k_1 = k_0\sqrt{\mu_{r_1}\epsilon_{r_1}}$ and $k_2 = k_0\sqrt{\mu_{r_2}\epsilon_{r_2}}$, respectively, where k_0 is the wavenumber of the semiinfinite medium above the superstrate (this semiinfinite region is usually free-space), and μ_{ri}, ϵ_{ri} are the relative permeability and permittivity referred to that medium so that $\mu_i = \mu_0\mu_{ri}$ and $\epsilon_i = \epsilon_0\epsilon_{ri}$. The functions $F^{U,W}$ in (3) and (4) can be determined by solving the boundary-value problem in the spectral domain, yielding (for $0 \le z, z' \le d_2$):

$$F^U(\xi) = \frac{\xi}{2k_{2z}}\left\{\frac{T_1^e\beta_1 + T_2^e\beta_2 + T_3^e\beta_3}{D_e}\right\} \tag{6}$$

where the T^e terms are given by:

$$T_1^e = D_{e1}^-(1 + \alpha_e) - D_{e1}^+(1 - \alpha_e)e^{-2jk_{2z}d_2} \tag{7}$$

$$T_2^e = D_{e1}^+\{1 + \alpha_e + (1 - \alpha_e)e^{-2jk_{2z}(d_2 - z')}\} \tag{8}$$

$$T_3^e = \left\{D_{e_1}^- + D_{e_1}^+ e^{-2jk_{2z}z'}\right\}(1 - \alpha_e)e^{-2jk_{2z}}\, d_2 \tag{9}$$

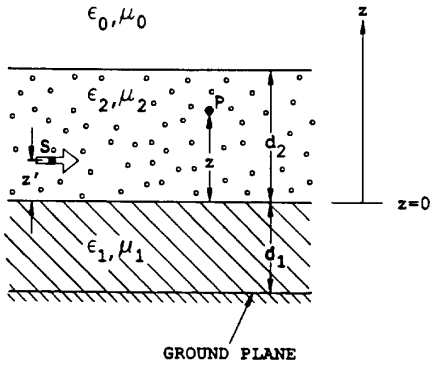

Fig. 1. Grounded double-layer configuration with source S (a horizontal electric dipole) and observation point P embedded in the superstrate.

and

$$D_{e1}^{\pm} = \frac{k_{2z}}{\mu_2} \pm j\frac{k_{1z}}{\mu_1}\cot[k_{1z}\, d_1] \tag{10}$$

$$\alpha_e = \frac{k_{0z}/\mu_0}{k_{2z}/\mu_2} \tag{11}$$

$$\beta_1 = e^{-j\delta_s k_{2z}(z - z')}; \qquad \delta_s = \begin{cases} 1 & z > z' \\ -1 & z < z' \end{cases} \tag{12}$$

$$\beta_2 = e^{-jk_{2z}(z + z')}; \qquad \beta_3 = e^{+jk_{2z}(z + z')} \tag{13}$$

being

$$k_{0z} = \sqrt{k_0^2 - \xi^2}; \qquad k_{1z} = \sqrt{k_1^2 - \xi^2};$$
$$k_{2z} = \sqrt{k_2^2 - \xi^2}. \tag{14}$$

It is noted that to be consistent with the Sommerfeld radiation condition the choice of the branch in (14) must be such that

$$\mathrm{Im}\{k_{0z}\} < 0. \tag{15}$$

Finally, the denominator in (6) is given by

$$D_e = \left\{\left(\frac{k_{2z}}{\mu_2}\right)^2 - j\frac{k_{0z}k_{1z}}{\mu_0\mu_1}\cot[k_{1z}\, d_1]\right\}\left\{\frac{1 - e^{-2jk_{2z}d_2}}{k_{2z}/\mu_2}\right\} + \left\{\frac{k_{0z}}{\mu_0} - j\frac{k_{1z}}{\mu_1}\cot[k_{1z}\, d_1]\right\}(1 + e^{-2jk_{2z}d_2}). \tag{16}$$

Similarly, F^W can be written as

$$F^W(\xi) = \frac{k_{2z}}{2\xi}\left\{\frac{T_1^m\beta_1 + T_2^m\beta_2 - T_3^m\beta_3}{D_m} - \frac{T_1^e\beta_1 + T_2^e\beta_2 + T_3^e\beta_3}{D_e}\right\} \tag{17}$$

with

$$T_1^m = D_{m1}^+(1 + \alpha_m) - D_{m1}^-(1 - \alpha_m)e^{-2jk_{2z}d_2} \tag{18}$$

$$T_2^m = D_{m1}^-\left[-(1 + \alpha_m) + (1 - \alpha_m)e^{-2jk_{2z}(d_2 - z')}\right] \tag{19}$$

$$T_3^m = \left[D_{m1}^+ - D_{m1}^- e^{-2jk_{2z}z'}\right](1 - \alpha_m)e^{-2jk_{2z}d_2} \tag{20}$$

and

$$D_{m1}^{\pm} = \frac{k_{2z}}{\epsilon_2} \pm \frac{k_{1z}}{\epsilon_1} j \tan[k_{1z} d_1] \tag{21}$$

$$\alpha_m = \frac{k_{0z}/\epsilon_0}{k_{2z}/\epsilon_2}. \tag{22}$$

The denominator D_m in (17) is now

$$D_m = \left\{ \left(\frac{k_{2z}}{\epsilon_2} \right)^2 + j \frac{k_{0z} k_{1z}}{\epsilon_0 \epsilon_1} \tan[k_{1z} d_1] \right\} \frac{(1 - e^{-2jk_{2z}d_2})}{k_{2z}/\epsilon_2} + \left\{ \frac{k_{0z}}{\epsilon_0} + j \frac{k_{1z}}{\epsilon_1} \tan[k_{1z} d_1] \right\} (1 + e^{-2jk_{2z}d_2}). \tag{23}$$

The above expressions for the fields have been checked to reduce to the single-layer case when μ_2, ϵ_2 tend to μ_0, ϵ_0 and/or d_2 tends to zero. Also, the denominators (16) and (23) agree with those given in [2], except for a multiplicative factor.

III. Pole Structure

The zeros of D_e, D_m in (6) and (17) constitute the poles of the composite (double) layer. Their number and location depend on the layer thicknesses and material constants, as well as the wavenumber k_0. Restricting our attention to the lossless case, it is well known that D_e, D_m exhibit a certain number of zeros on the real axis of the ξ-plane, in the interval $[k_0, \max(k_1, k_2)]$. These poles describe the surface waves guided by the structure, and therefore appear on the proper Riemmann sheet (consistent with the radiation condition) of the ξ-plane, as defined in (15). But there are also poles on the improper Riemmann sheet of the ξ-plane, known as leaky wave poles. Although there are in general an infinite number of them [12], it was found in [10] and [13] for the single-layer case that the inclusion of only a particular set of these poles produced a significant improvement in the asymptotic solution, for nearby source and observation points on the surface of the slab. This set of poles is located on the real axis of the improper Riemmann sheet of the ξ-plane for the lossless case, and therefore they will be referred to as improper surface wave poles. It was also found that proper and improper surface wave poles are closely related. In fact, surface wave poles (except for the first TM surface wave pole, which is always above cutoff) are originally improper poles that move towards the branch cut at k_0 along the real axis of the improper Riemmann sheet as the layer thickness increases, and finally "jump" into the proper plane, then moving away from k_0 along the proper real axis. In the same way, improper surface wave poles are originally improper complex (or leaky wave) poles that move onto the improper real axis when the appropriate conditions are met. In this section, we will investigate the number of TE and TM poles on the real axes of both, the proper and improper sheets (ξ-plane) for a general double layer structure, as a function of its constitutive parameters. Also, a simple procedure to locate the first TE and TM proper and/or improper surface wave poles will be outlined.

A. Zeros of D_e

As mentioned before, a new TE surface wave pole will always appear initially at $\xi = k_0$ on the proper Riemmann sheet, so the following condition must be met:

$$D_e(\xi = k_0) = 0 \tag{24}$$

which can be written using (16) as

$$\frac{\sqrt{n_2 - 1}}{\mu_{r2}} \tan\left[k_0 d_2 \sqrt{n_2 - 1}\right] = \frac{\sqrt{n_1 - 1}}{\mu_{r1}} \cot\left[k_0 d_1 \sqrt{n_1 - 1}\right] \tag{25}$$

where $n_1 = \epsilon_{r1} \mu_{r1}$; $n_2 = \epsilon_{r2} \mu_{r2}$. Defining, in a way similar to [12], the parameters $L_1 = k_0 d_1 \sqrt{n_1 - 1}$, $L_2 = k_0 d_2 \sqrt{n_2 - 1}$, (25) can be expressed more compactly as

$$\frac{\sqrt{n_2 - 1}}{\mu_{r2}} \tan(L_2) = \frac{\sqrt{n_1 - 1}}{\mu_{r1}} \cot(L_1). \tag{26}$$

It is noted that this equation was already given by Jackson and Alexopoulos [1, eq. (37)], and it represents the condition for any TE surface wave mode to turn on. For example, for a given $\epsilon_{r2}, \mu_{r2}, d_2$ such that $L_2 < \pi/2$, (26) will be satisfied at infinite points, each one for a certain L_1 such that $N\pi < L_1 z(2N + 1)\pi$ with $(N = 0, 1, 2, \cdots)$. If we plot the condition (26) in a two-dimensional $L_1 L_2$ plane for a given set of ϵ_{ri}, μ_{ri}, we get a plot like in Fig. 2(a). In the regions between two consecutive curves, the number of surface waves is constant. However, the number of improper surface wave poles (lwp in Fig. 2) is not. As discussed before, two leaky wave poles move onto the improper real axis when the point defined by (L_1, L_2) in Fig. 2(a) moves close enough to the curve defining the order of the next region. As L_1 or L_2 increases, one of these poles begins moving towards the branch cut and finally "jumps" onto the proper Riemmann sheet, thus constituting a new surface wave pole.

Note in Fig. 2(a) that, if $\epsilon_{r2} = \mu_{r2} = 1$ (no second layer present), $L_2 = 0$ and the L_1, L_2 plane reduces to the L_1 axis, yielding the results already reported in [12] for the single-layer case. It is also noted that the curved segments between dots in Fig. 2 can be convex or concave, depending on the particular values of ϵ_{ri}, μ_{ri} in (26).

In most practical configurations, there is only one proper or improper TE surface wave pole, and it can be easily found as follows. The pole will be located on the real axis of the proper (improper) sheet if the left-hand side of (26) is greater (smaller) than the right-hand side. In either case, a Newton–Raphson searching procedure implemented in (16) with $\xi_{is} = 0.99 k_0 \sqrt{n_2}$ (for a swp) or $\xi_{il} = k_0$ (for a lwp) as initial value has been found to provide the actual location of the pole in only a few iterations. Note that the subscript *is* on ξ_{is} above refers to the value of

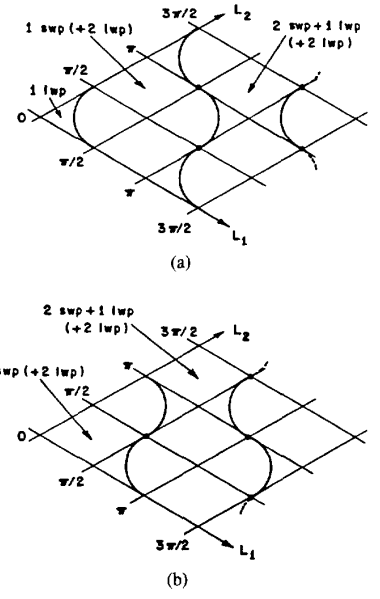

Fig. 2. Number of proper (swp) and improper (lwp) surface wave poles for given materials (ϵ_{ri}, μ_{ri}), as a function of layer thicknesses: (a) TE case, and (b) TM case ($L_1 = k_0 d_1 \sqrt{\epsilon_{r_1}\mu_{r_1} - 1}$, $L_2 = k_0 d_2 \sqrt{\epsilon_{r_2}\mu_{r_2} - 1}$). The number of lwp indicated within the brackets are additional improper surface wave poles that can exist in each region.

the initial guess for the location (in the ξ plane) of the proper surface wave pole, and likewise the subscript *il* on ξ_{il} refers to the initial value of ξ pertaining to the improper surface wave pole.

B. Zeros of D_m

Similar considerations to those discussed in the previous case lead now to the following condition, for a TM pole to arise on the proper Riemmann sheet

$$\frac{\sqrt{n_2 - 1}}{\epsilon_{r2}} \tan(L_2) = -\frac{\sqrt{n_1 - 1}}{\epsilon_{r1}} \tan(L_1) \quad (27)$$

We can again plot the condition (27) in an L_1, L_2 plane, as we did for D_e. The result for a given set of ϵ_{ri}, μ_{ri} is shown in Fig. 2(b). The same general considerations discussed above for D_e are applicable here. It is also seen that, for $L_2 = 0$ (single layer case), the plane in Fig. 2(a) reduces to the L_1 axis, with the result already given in [12].

In most practical double layer structures, there is only one TM surface wave pole, although two leaky wave poles may also exist on the improper real ξ-axis. This situation corresponds to the first region in Fig. 2(b). The surface wave pole can be found by implementing a Newton–Raphson search procedure in (23) with $\xi_{is} = 0.99k_0\sqrt{n_2}$ as a starting value. The improper surface wave poles (if any) can be located in a similar manner, now starting the search at both $\xi_{l1} = k_0$ and $\xi_{l2} = 0.99k_0\sqrt{n_2}$. The ξ_{l1} and ξ_{l2} above represent the values of the initial guesses for the location in the ξ plane of the first and second improper surface wave poles, respectively. When $L_1 > \pi/2$, D_m presents a singularity at $d_1\sqrt{k_1^2 - \xi_s^2} = \pi/2$. In this case special care must be taken with the starting value of the searching algorithm in both Riemmann sheets, because the searching procedure cannot "cross" a singularity. These situations can be easily handled by plotting D_m along both (proper and improper) real ξ-axes to determine appropriate starting values.

IV. Asymptotic Evaluation of the Sommerfeld Integrals

Conventional numerical evaluation of the Sommerfeld-type integrals (3), (4) presents two main difficulties. First, the integrands exhibit a certain number of poles that have to be extracted in order to obtain a relatively smooth function suitable for numerical integration. Second, the oscillatory, slowly decaying behavior of the Bessel function results in a poor convergence of the integrals, particularly when the lateral separation between source and observation points is large in terms of the wavelength.

To overcome these limitations, asymptotic closed-form expressions for U and W in (3) and (4) will be developed in this section. To carry out the asymptotic evaluation we first write integrals (3) and (4), due to the oddness of $F^{U,W}$ with respect to ξ, as:

$$U = \frac{1}{2}\int_{C_s} F^U(\xi) H_0^{(2)}(\rho\xi)\, d\xi \quad (28)$$

$$W = \frac{1}{2}\int_{C_s} F^W(\xi) H_0^{(2)}(\rho\xi)\, d\xi \quad (29)$$

where C_s is the Sommerfeld path, as shown in Fig. 3. This path can be deformed to give the sum of the enclosed residues plus the integral around the branch cut (contour C_B in Fig. 3):

$$U = -\frac{1}{2}\sum_i 2\pi j R^U(\xi_i) H_0^{(2)}(\rho\xi_i) + \frac{1}{2}\int_{C_B} F^U(\xi) H_0^{(2)}(\rho\xi)\, d\xi \quad (30)$$

$$W = -\frac{1}{2}\sum_i 2\pi j R^W(\xi_i) H_0^{(2)}(\rho\xi_i) + \frac{1}{2}\int_{C_B} F^W(\xi) H_0^{(2)}(\rho\xi)\, d\xi. \quad (31)$$

Here, $R^{U,W}$ are the residues of $F^{U,W}$ at $\xi = \xi_i$ (proper surface wave poles), and can be calculated as follows:

$$R^U(\xi_i) = \lim_{\xi\to\xi_i}(\xi - \xi_i)F^U(\xi) = \frac{N^U(\xi_i)}{D_e'(\xi_i)} \quad (32)$$

$$R^W(\xi_i) = \lim_{\xi\to\xi_i}(\xi - \xi_i)F^W(\xi) = \frac{N^W(\xi_i)}{D_{ns}(\xi_i)\cdot D_s'(\xi_i)} \quad (33)$$

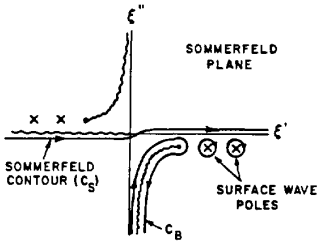

Fig. 3. Original Sommerfeld contour (C_S), and the deformation to give the sum of the enclosed residues plus the integral around the branch cut (C_B). Here, $\xi = \xi + j\xi''$.

where $N^{U,W}$ represent the numerators of F^U and F^W in (6) and (17) and D_s, D_{ns} stand for the singular and nonsingular denominators in (17). The minus sign of the residues in (30) and (31) comes from clockwise integration around the poles.

The above result, (30), (31), allows for the interpretation of the solution in terms of two contributions: a discrete number of surface waves, whose strengths are given by the corresponding residues at the poles, plus a continuous spectrum of waves, represented by the integral around the branch cut. The purpose of the asymptotic evaluation is to obtain the dominant terms in the latter.

With the above view in mind, the following changes of variable can be used [9]–[11]:

$$\tau = \sqrt{k_0^2 - \xi^2} \tag{34}$$

$$\cos\gamma = \frac{\tau}{k_0} \tag{35}$$

$$\sin\gamma = 1 - js^2. \tag{36}$$

The first one transforms the integral around the branch cut into a real-axis integral in the τ plane. The second performs the angular spectrum mapping, and the third transforms the steepest descent path (SDP) in the γ plane onto the real axis of the s-plane. The three planes, as well as the paths of integration and the location of proper and improper surface wave poles (lossless case) are shown in Fig. 4.

Since the above transformations have been discussed in more detail in [9]–[11], it will thus suffice for our purposes to consider the direct transformation from the ξ-plane to the s-plane:

$$\xi = k_0(1 - js^2). \tag{37}$$

Introducing the above transformation in a general integral of the form

$$I_B = \frac{1}{2}\int_{C_B} F(\xi) H_0^{(2)}(\rho\xi)\, d\xi \tag{38}$$

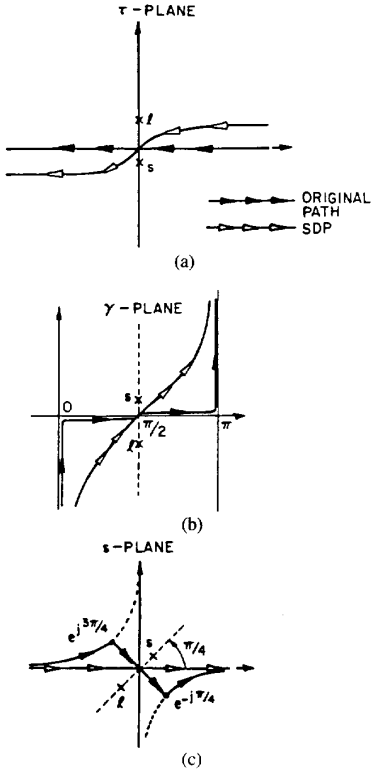

Fig. 4. Original and steepest descent (SDP) paths of integration in the (a) τ-plane; (b) γ-plane; and (c) s-plane. The location of proper (s) and improper (l) surface wave poles is also shown.

where C_B is the contour shown in Fig. 2, one gets

$$I_B = \frac{1}{2}\int_{\Gamma_0^s} F\left[k_0(1-js^2)\right] H_0^{(2)}\left[k_0\rho(1-js^2)\right](-2jk_0 s)\, ds \tag{39}$$

where Γ_0^s is the resulting contour of integration in the s-plane, as shown in Fig. 4(c). Now, if $k_0\rho$ is assumed to be large, we can use the large-argument form of the Hankel function in (39), yielding

$$I_B \sim \frac{1}{2}\sqrt{\frac{2k_0}{\pi\rho}}\, e^{j(\pi/4)} e^{-jk_0\rho}\int_{\Gamma_0^s} G(s) e^{-k_0\rho s^2}\, ds \tag{40}$$

where

$$G(s) = F\left[k_0(1-js^2)\right]\frac{-2js}{\sqrt{1-js^2}} \tag{41}$$

By deforming the original contour Γ_0^s into Γ_{SDP}^s, extracting the singularities and approximating the resulting regular function by the first two nonvanishing terms of its Taylor series expansion around $s = 0$ [14], [15], one gets the following result:

$$I_B \sim \frac{e^{j(\pi/4)}}{\sqrt{2}}\frac{e^{-jk_0\rho}}{\rho}\left[\sum_i \frac{R(b_i)}{b_i}\left[1 - \tilde{F}(jk_0\rho b_i^2)\right] + \frac{1}{2k_0\rho}\left\{\frac{G''(0)}{2} + \sum_i \frac{R(b_i)}{b_i^3}\right\}\right] \tag{42}$$

where $R(b_i)$ are the residues of $G(s)$ at $s = b_i$ (singularities in the s-plane), $G''(0)$ is the second-order derivative of (41) evaluated at $s = 0$ and $\tilde{F}(x)$ is the transition function (as defined in [11]).

It can be easily shown that the residues of $G(s)$ at $s = b_i$ are related to those of $F(\xi)$ at $\xi = \xi_i$ by

$$R(b_i) = \frac{R(\xi_i)}{\sqrt{k_0 \xi_i}} \tag{43}$$

where $R(\xi_i)$ is defined in (32) and (33), and

$$b_i = e^{j(\pi/4)}\sqrt{\xi_i/k_0 - 1} \tag{44}$$

where the principal branch of the above square root ($\mathrm{Re}(b_i) > 0$) corresponds to surface wave poles, and the other branch to leaky wave poles.

It can be seen that the solution given in (42) is in a very amenable format, involving only simple algebraic operations and the well-known transition function $\tilde{F}$, which contains simple Fresnel integrals in the lossless case [11]. Also, the summations in (42) involve only one or two poles in most practical cases (which typically involve only moderately thin layers). The evaluation of the second derivative of (41) at $s = 0$ is also simplified by noting that:

$$G''(s = 0) = -4jF'(s = 0) \tag{45}$$

where F is $F^{U,W}(\xi)$ in (6) or (17) evaluated at $\xi = k_0(1 - js^2)$. Although somewhat cumbersome due to the relatively functions involved, the evaluation of $F'(s = 0)$ in (45) is straightforward, and the results for three different situations (source and observation points both along the first or second interface and along different interfaces) are given in Appendix A.

It must be mentioned at this point that a complex leaky wave pole existing on the improper sheet of the original ξ-plane may contribute to the solution if it is captured in the path deformation (Γ_0^r into Γ_{SDP}^s), or it may still influence the solution if it appears close enough to the saddle point. In these cases, the asymptotic solution including only the real ξ-axis proper and improper surface wave poles will be seen to lose accuracy in the neighborhood of the source. However, this can be regarded as a second-order effect, since the complex leaky wave poles cannot appear arbitrarily close to the saddle point, while real-axis poles do. Nevertheless, these situations are rarely found in practice.

Finally, when the observation point is very close to the source, the asymptotic solution will fail, and a numerical integration procedure (see e.g., [11]) or alternative integral representations [16] must be used.

V. Numerical Results and Conclusions

In this section we will first examine the accuracy of the asymptotic approximation in the three cases considered in the Appendix. The examples have been selected to show the validity of the closed-form expressions for different combinations of low and high dielectric constants, as well as thin and thick dielectric slabs (lossless case). Although magnetic materials will not be used throughout these examples, it must be mentioned that there is no essential difference in the treatment of the magnetic material and the dielectric material from a purely numerical point of view, and the asymptotic solution is equally valid for both.

In the examples shown below, one TM surface wave pole (plus two improper surface wave poles when necessary) and one TE proper or improper surface wave pole have been included in the asymptotic solution. Thus, Fig. 5 shows a comparison between the numerical evaluation of the exact W (4) and its asymptotic approximation [(31) and (42)], versus lateral separation between source and observation points. The "exact" value of the function U and W is always calculated by a numerical (Gaussian) integration of (3) and (4), once the limiting behavior and singularities of the integrand have been extracted [11]. In this case, the source and observation points are located on the interface between the two dielectric layers. As can be seen, the asymptotic closed-form expression remains valid for lateral distances as small as two tenths of the free-space wavelength λ_0. Also, Table I shows a CPU time comparison between the calculation based on the numerical integration procedure and the asymptotic closed-form expressions. It is apparent that the use of the closed-form result in conjunction with any spatial-domain formulation will result in a substantial savings of computer time. It must also be mentioned that, in all the cases studied here, the accuracy of the asymptotic approximation for U is at least as good as it is for W.

Another example is shown in Fig. 6 in which a thin, low dielectric constant slab is placed on top of a moderately thick, high dielectric constant layer. In this case, the source and observation points are along different interfaces. Again, the asymptotic solution remains valid for lateral distances of the order of $0.4\lambda_0$, although probably $0.2\lambda_0$ could be used for most practical purposes. In this case, there is no singularity when $\rho \to 0$, because the source and observation points are at least separated by the thickness of the second (superstrate) layer.

One more representative case is shown in Fig. 7, where a thick layer is now placed on top of a thin one, both with high dielectric constants. Source and observation points are here along the dielectric–air interface. As can be seen, the asymptotic solution can be used in this case almost down to one tenth of the free-space wavelength.

In general it can be said that the asymptotic closed-form expressions for U and W can be used down to a few tenths of the free-space wavelength, for source and observation points along the same or different interfaces. This also applies if source and/or observation points are embedded somewhere inside the layers. However, as it was mentioned before, in those particular situations in which a complex leaky wave pole contributes significantly to the asymptotic solution, the above expressions for U and W converge at large lateral distances from the source, of the order of one free-space wavelength. However, this restriction in the asymptotic solution can be eliminated even in the latter case if the effect of such complex leaky wave

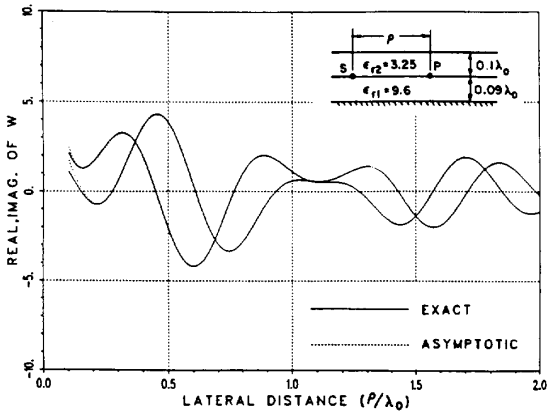

Fig. 5. Comparison between the exact W and its asymptotic approximation, for source and observation points both along the first interface.

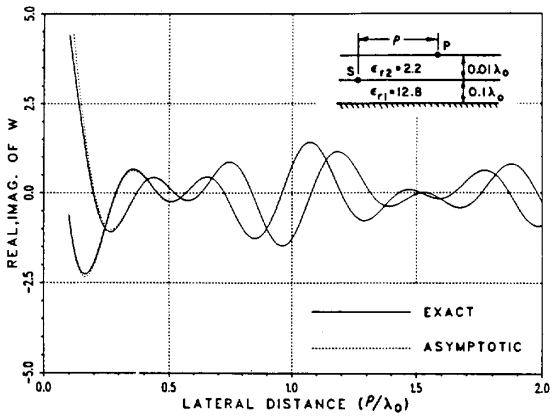

Fig. 6. Comparison between exact and asymptotic W in another example. In this case, source and observation points are along different interfaces.

TABLE I
CPU TIME (MILLISECONDS IN A VAX 8550) TO CALCULATE BOTH U AND W AT SEVERAL DISTANCES FROM THE SOURCE IN THE EXAMPLE OF FIG. 5

Lateral distance (ρ/λ_0)	CPU time numerical integration	CPU time asymptotic closed-form
0.5	84	4
1.0	145	4
2.0	176	4

poles is incorporated into the solution in a manner similar to that done for the improper surface wave poles.

On the other hand, computational efficiency is not the only advantage of an asymptotic solution. It also provides physical insight into the field behavior, giving separate contributions that vividly highlight the different wave phenomena. Thus, the interference between the space wave and the pole wave transition effects is contained in (42), whereas the effect of proper surface wave poles is explicitly represented by the residue terms in (30) and (31). As

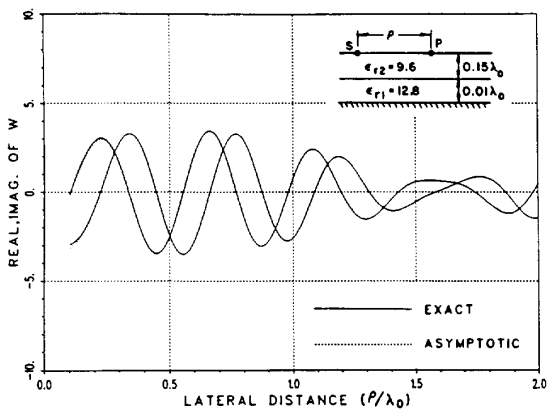

Fig. 7. Exact and asymptotic W for a case in which both source and observation points are along the dielectric-air interface.

an example, it is known that a TM surface wave can be eliminated by using a superstrate (cover) under certain conditions [1]. It turns out that for nonmagnetic superstrates, the surface wave elimination is only possible when the substrate is very thin, whereas the use of a magnetic second layer allows for much thicker substrates. These facts can be easily shown by plotting the residue (33) at the first TM surface wave pole. This residue actually represents the "strength" with which the TM surface wave is excited, and therefore will vanish when the appropriate conditions are met. Fig. 8 shows an example in which the absolute value of the TM residue (case 1 of the Appendix) is plotted versus superstrate thickness, for both a magnetic and a non-magnetic superstrate. As can be seen, the surface wave residue for the magnetic superstrate[1] exhibits a zero at $d_2 = 0.02\lambda_0$, while in the nonmagnetic case there is no such phenomena. It is noted that both residues reduce to the single-layer case when $d_2 \to 0$. It must also be mentioned that, for the nonmagnetic superstrate, the next (TE) surface wave arises at $d_2 = 0.033\lambda_0$, while for the magnetic case this occurs at $d_2 = 0.07\lambda_0$.

Also, by using the asymptotic closed-form expressions, we can easily plot the fields produced by an elementary source. Let us imagine an $\hat{x}$-directed elementary electric dipole in a double-layer structure. If the observation point moves around the source in a circumference of radius R (in the plane of the source), using (1) and (2) we can calculate the E_{xx} and E_{yx} "planar" radiation patterns, as a function of the aspect angle ϕ with the $\hat{x}$-axis. Fig. 9 shows the results for a structure that supports only one TM surface wave, which produces a lobe of E_{xx} in the endfire direction (note that in free space such a lobe will appear in the broadside direction). However, when another (now TE) surface wave is present, a second lobe appears around $\phi = 90°$, as shown in Fig. 10. In these examples the derivatives in (1) and (2) were evaluated numerically, but for R large enough to where only the

[1]Results for the mutual impedance between two printed dipoles in this particular case are presented in [7], Fig. 8.

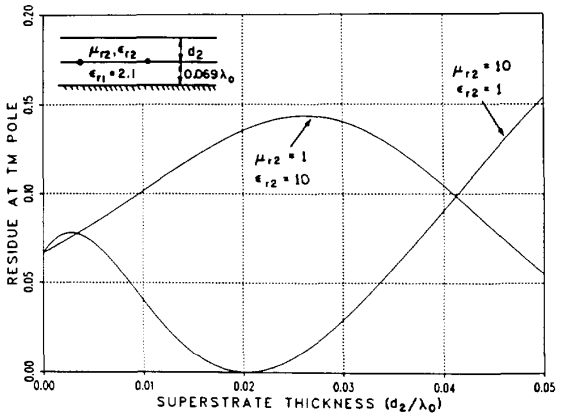

Fig. 8. Residue at the TM surface wave pole for a magnetic ($\mu_{r_2} = 10$, $\epsilon_{r_2} = 1$) and a non-magnetic ($\epsilon_{r_2} = 10$, $\mu_{r_2} = 1$) superstrate, versus superstrate thickness.

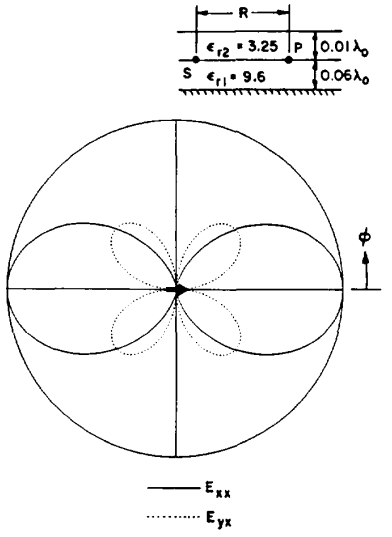

Fig. 9. Normalized surface fields E_{xx}, E_{yx} produced by an elementary electric dipole at a distance R, versus $\phi (R = 5\lambda_0)$. In this case, only a TM surface wave exists.

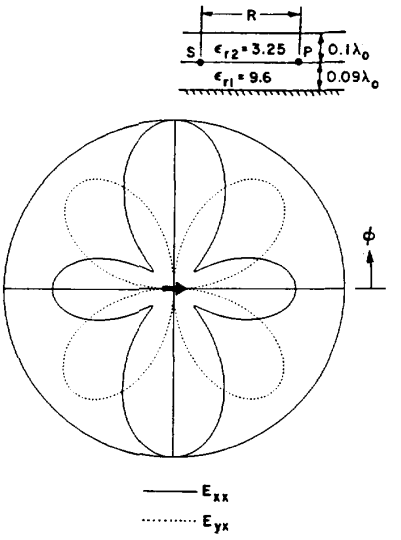

Fig. 10. Normalized surface fields produced by an elementary electric dipole at an observation point (R, ϕ) versus $\phi (R = 5\lambda_0)$. In this case both a TE and a TM surface wave exist.

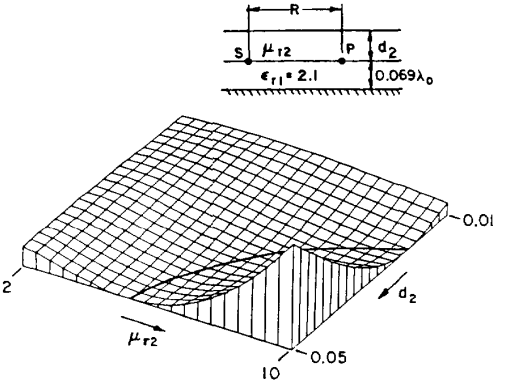

Fig. 11. Magnitude of the E_{xx} field produced by an elementary electric dipole at $R = 5\lambda$, $\phi = 0$ as a function of both superstrate permeability and thickness. The solid line shows the locus of the combinations μ_{r_2}, d_2 that eliminate the first TM surface wave ($\epsilon_{r_2} = 1$).

surface waves [first terms in (30) and (31)] need to be considered. It can be done analytically, yielding $\sin^2 \phi$ or $\cos^2 \phi$ type patterns corresponding to the TE or TM surface wave poles, respectively.

Finally, since the calculation of the field produced by an elementary source is extremely efficient in terms of computer time, it allows for parametric studies, like the one shown in Fig. 11. In this example, the E_{xx} field produced by an elementary source at $R = 5\lambda_0$, $\phi = 0$ is plotted as a function of both the relative permeability and thickness of the superstrate. The line shown in the figure represents the locus of the combinations (μ_{r2}, d_2) that eliminate the first TM surface wave. As can be seen, the "cut" of the above figure defined by $\mu_{r2} = 10$ is the one already shown in Fig. 8.

In conclusion, an asymptotic closed-form approximation for the Green's function of a horizontal electric dipole in a grounded double-layer configuration has been derived. This representation is valid for source and observation points anywhere in the superstrate (including interfaces), although it can be easily extended to cases in which source and/or observation points are in the substrate. The large parameter in the asymptotic approximation is the lateral separation between source and observation points, and the asymptotic solution has been checked to agree with the exact Green's function for lateral separations down to a few tenths of the free-space wavelength. Also, the usefulness of the asymptotic expressions has been demonstrated with illustrative examples. It is noted that the present asymptotic procedure can, in principle, be generalized to n layers; however, the n layer case would

require one to perform certain differentiations in the s plane (as in the Appendix for $n = 2$ case), which can become far more cumbersome than for the $n = 2$ case, if done analytically. At present, we are looking at efficient numerical procedures to overcome this difficult problem in the generalization to n layers. It is believed that these asymptotic closed-form expressions can greatly improve the efficiency of the present methods of analyzing printed circuits/antennas, as well as contribute to a better understanding of the related phenomena.

Appendix. Derivatives in the S-Plane

The calculation of derivatives in the s-plane can be done in the general case as follows. We first write $F^{U,W}$ in (6) and (17) using (37) as

$$F^{U}\left[\xi = k_0(1 - js^2)\right] = \frac{N^{U}(s)}{D_e(s)} \tag{A.1}$$

$$F^{W}\left[\xi = k_0(1 - js^2)\right] = \frac{N_m^{W}(s)}{D_m(s)} - \frac{N_e^{W}(s)}{D_e(s)} \tag{A.2}$$

where $D_e(\xi), D_m(\xi)$ are given in (16) and (23); and $N^{U}, N_{e,m}^{W}$ are simply found by comparing (A.1) and (A.2) with (6) and (17). Now the problem has been reduced to compute derivatives of the form:

$$F'(s) = \frac{\partial}{\partial s}\frac{N(s)}{D(s)} = \frac{N'(s)\cdot D(s) - N(s)D'(s)}{D^2(s)}. \tag{A.3}$$

Since we are only interested in the derivatives at $s = 0$ (i.e., $\xi = k_0$), the above formula simplified to:

$$F'(s=0) = \frac{N'(s=0)\cdot D(\xi = k_0) - N(\xi = k_0)\cdot D'(s=0)}{D^2(\xi = k_0)}. \tag{A.4}$$

Using the formulas in Section II, N^{U}, $N_{e,m}^{W}$, and $D_{e,m}$ at $\xi = k_0$ are easily found. The only remaining quantities to evaluate in (A.4) are the first derivatives of N^{U}, $N_{e,m}^{W}$, and $D_{e,m}$ at $s = 0$. These are given by:

$$D_e'(s=0) = \left(-k_0\sqrt{2}\,e^{j(\pi/4)}\right)\cdot\left[-\frac{j}{\mu_1}\left\{\frac{\sqrt{n_1-1}}{\tan\left(k_0 d_1\sqrt{n_1-1}\right)}\right\}\frac{\mu_2}{\sqrt{n_2-1}}\cdot\left(1 - e^{-2jk_0 d_2\sqrt{n_2-1}}\right) + 1 + e^{-2jk_0 d_2\sqrt{n_2-1}}\right] \tag{A.5}$$

$$D_m'(s=0) = \left(-k_0\sqrt{2}\,e^{j(\pi/4)}\right)\left[\frac{j}{\epsilon_1}\left\{\sqrt{n_1-1}\tan\left(k_0 d_1\sqrt{n_1-1}\right)\right\}\cdot\frac{\epsilon_2}{\sqrt{n_2-1}}\left(1 - e^{-2jk_0 d_2\sqrt{n_2-1}}\right) + 1 + e^{-2jk_0 d_2\sqrt{n_2-1}}\right]. \tag{A.6}$$

Note that D_e, D_m do not depend on the position of source and/or observation point, so their values at $\xi = k_0$ and their derivatives at $s = 0$ do not need to be changed in the cases described below.

Case 1. Source and Observation Points Both Along the First Interface ($z' = o$, $z = o$):

$$N^{U'}(s=0) = -k_0\sqrt{2}\,e^{j(\pi/4)}\frac{1 - e^{-2jk_0 d_2\sqrt{n_2-1}}}{\sqrt{n_2-1}} \tag{A.7a}$$

$$N_e^{W'}(s=0) = -k_0\sqrt{2}\,e^{j(\pi/4)}\sqrt{n_2-1}\left(1 - e^{-2jk_0 d_2\sqrt{n_2-1}}\right) \tag{A.7b}$$

$$N_m^{W'}(s=0) = -jk_0\sqrt{2}\,e^{j(\pi/4)}\sqrt{n_1-1}\,\frac{\epsilon_2}{\epsilon_1}\tan\left(k_0 d_1\sqrt{n_1-1}\right)\cdot\left[1 + e^{-2jk_0 d_2\sqrt{n_2-1}}\right] \tag{A.7c}$$

Case 2. Source and Observation Points Along Different Interfaces ($z' = o$, $z = d_2$):

$$N^{U'}(s=0) = 0 \tag{A.8a}$$

$$N_e^{W'}(s=0) = 0 \tag{A.8b}$$

$$N_m^{W'}(s=0) = -jk_0\sqrt{2}\,e^{j(\pi/4)}\frac{\epsilon_2}{\epsilon_1}\sqrt{n_1-1}\tan\cdot\left(k_0 d_1\sqrt{n_1-1}\right)2e^{-jk_0 d_2\sqrt{n_2-1}} \tag{A.8c}$$

Case 3. Source and Observation Points Both Along the Second Interface ($z' = d_2$, $z = d_2$):

$$N^{U'}(s=0) = 0 \tag{A.9a}$$

$$N_e^{W'}(s=0) = 0 \tag{A.9b}$$

$$N_m^{W'}(s=0) = -k_0\sqrt{2}\,e^{j(\pi/4)}\left\{\sqrt{n_2-1}\left(1 - e^{-2jk_0 d_2\sqrt{n_2-1}}\right) + j\sqrt{n_1-1}\,\frac{\epsilon_2}{\epsilon_1}\tan\left(k_0 d_1\sqrt{n_1-1}\right)\cdot\left(1 + e^{-2jk_0 d_2\sqrt{n_2-1}}\right)\right\} \tag{A.9c}$$

Acknowledgment

The authors gratefully acknowledge Sina Barkeshli for numerous helpful and stimulating discussions.

References

[1] N. G. Alexopoulos and D. R. Jackson, "Fundamental superstrate (cover) effects on printed circuit antennas," *IEEE Trans. Antennas Propagat.*, vol. AP-32, pp. 807–816, Aug. 1984.

[2] D. R. Jackson and N. G. Alexopoulos, "Gain enhancement methods for printed circuit antennas," *IEEE Trans. Antennas Propagat.*, vol. AP-33, pp. 976–987, Sept. 1985.

[3] I. E. Rana and N. G. Alexopoulos, "Current distribution and input impedance of printed dipoles," *IEEE Trans. Antennas Propagat.*, vol. AP-29, pp. 99–106, Jan. 1981.

[4] D. M. Pozar, "Input impedance and mutual coupling of rectangular microstrip antennas," *IEEE Trans. Antennas Propagat.*, vol. AP-30, pp. 1191–1196, Nov. 1982.
[5] P. B. Katehi and N. G. Alexopoulos, "Frequency-dependent characteristics of microstrip discontinuities in millimeter-wave integrated circuits," *IEEE Trans. Microwave Theory Tech.*, vol. MTT-33, pp. 1029–1035, Oct. 1985.
[6] R. W. Jackson and D. M. Pozar, "Full-wave analysis of microstrip open-end and gap discontinuities," *IEEE Trans. Microwave Theory Tech.*, vol. MTT-33, pp. 1036–1042, Oct. 1985.
[7] D. R. Jackson and N. G. Alexopoulos, "Analysis of planar strip geometries in a substrate–superstrate configuration," *IEEE Trans. Antennas Propagat.*, vol. AP-34, pp. 1430–1438, Dec. 1986.
[8] J. R. Mosig, "Arbitrarily shaped microstrip structures and their analysis with a mixed potential integral equation," *IEEE Trans. Antennas Propagat.*, vol. AP-36, pp. 314–323, Feb. 1988.
[9] S. Barkeshli, "An efficient approach for evaluating the planar microstrip Green's function and its applications to the analysis of microstrip antennas and arrays," Ph.D. dissertation, The Ohio State Univ., Dept. of Elect. Eng., Columbus, OH, 1988.
[10] S. Barkeshli, P. H. Pathak, and M. Marin, "An asymptotic closed form microstrip surface Green's function for the efficient moment method analysis of mutual coupling in microstrip antenna arrays," *IEEE Trans. Antennas Propagat.*, vol. AP-38, no. 9, pp. 1374–1383, Sept. 1990.
[11] M. Marin, S. Barkeshli, and P. H. Pathak, "Efficient analysis of planar microstrip geometries using an asymptotic closed-form of the grounded dielectric slab Green's function," *IEEE Trans. Microwave Theory Tech.*, vol. MTT-37, no. 4, pp. 669–678, Apr. 1989.
[12] R. E. Collin, *Field Theory of Guided Waves*. New York: McGraw-Hill, 1960.
[13] M. Marin, S. Barkeshli, and P. H. Pathak, "On the location of surface and leaky wave poles for the grounded dielectric slab," *IEEE Trans. Antennas Propagat.*, vol. AP-38, pp. 570–573, Apr. 1990.
[14] L. B. Felsen and N. Marcuvitz, *Radiation and Scattering of Waves*. Englewood Cliffs, NJ: Prentice-Hall, 1973.
[15] R. G. Rojas, "Comparison between two asymptotic methods," *IEEE Trans. Antennas Propagat.*, vol. AP-35, pp. 1489–1492, Dec. 1987.
[16] S. Barkeshli and P. H. Pathak, "Radially propagating and steepest descent path integral representations of the planar microstrip dyadic Green's function," *Radio Sci.*, vol. 25, no. 2, pp. 161–174, Mar.–Apr. 1990.

M. A. Marin (M'87) for a photograph and biography please see page 1383 of the September 1990 issue of this TRANSACTIONS.

Prabhakar H. Pathak (M'76–SM'81–F'86), for photograph and biography, please see page 4 of the January 1988 issue of this TRANSACTIONS.